

Femtosecond laser-induced size reduction and emission quantum yield enhancement of colloidal silicon nanocrystals: effect of laser ablation time

Y X Zhang¹, W S Wu¹, H L Hao¹  and W Z Shen²

¹ College of Material Engineering, Shanghai University of Engineering Science, 333 Long Teng Road, Shanghai 201620, People's Republic of China

² Institute of Solar Energy, and Key Laboratory of Artificial Structures and Quantum Control (Ministry of Education), Department of Physics and Astronomy, Shanghai Jiao Tong University, 800 Dong Chuan Road, Shanghai 200240, People's Republic of China

E-mail: sulee8866@126.com

Received 20 March 2018, revised 8 June 2018

Accepted for publication 19 June 2018

Published 3 July 2018



Abstract

Colloidal silicon (Si) nanocrystals (NCs) with different sizes were successfully prepared by femtosecond laser ablation under different laser ablation time (LAT). The mean size decreases from 4.23 to 1.42 nm by increasing the LAT from 30 to 120 min. In combination with structural characterization, temperature-dependent photoluminescence (PL), time-resolved PL and PL excitation spectra, we attribute room-temperature blue emissions peaked at 405 and 430 nm to the radiative recombination of electron–hole pairs via the oxygen-deficient centers related to Si–C–H₂ and Si–O–Si bonds of colloidal Si NCs prepared in 1-octene, respectively. In particular, the measured PL quantum yield of colloidal Si NCs has been enhanced significantly from 23.6% to 55.8% by prolonging the LAT from 30 to 120 min.

Keywords: laser ablation time, colloidal silicon nanocrystals, optical properties, photoluminescence quantum yield

(Some figures may appear in colour only in the online journal)

Colloidal silicon (Si) nanocrystals (NCs) have attracted significant interest owing to their fascinating optical properties, which cannot be exhibited by their bulk counterpart. When the dimensions of Si NCs are reduced below the Bohr radius of an exciton in Si (~ 4.5 nm) [1], their emission can be easily controlled by adjusting the Si NC size [2]. Due to the abundance and non-toxicity of Si, the application of Si in a broad range of opto-electronic devices presents more advantages than other elements. The efficient luminescence from Si has inspired us to pursue the continuous development of Si-based opto-electronic devices [3, 4] and bio-medical applications [5, 6].

It is generally accepted that the size of colloidal Si NCs has an important impact on the luminescence of colloidal Si NCs. In fact, the surface chemistry of Si NCs plays a

dominant role in their opto-electronic properties. For instance, the photoluminescence (PL) from Si NCs can be adjusted across the visible spectrum by changing the surface groups without changing their size [7–9]. For practical applications in opto-electronic devices and bio-medicine, it is necessary for Si NCs to have stable structure and optical properties. The organic molecules formed on the surface of Si NCs can prevent the agglomeration of Si NCs through steric barriers or electrostatic repulsion, and guarantee the high stability in solution and stable optical properties.

The laser ablation of solids in liquid (LAL) environment has proved to be a new and highly promising technique for preparing nano-colloids. This is due to its highly non-equilibrium processing, which allows the synthesis of nano-structured materials. The LAL technique makes it easy to prepare

the nano-colloids and eliminate the contamination by a reducing agent. Several laser parameters are very important to control the size and structure of the nanoparticles. Recently, the effect of pulse energy on the size and stability of Si nanoparticles has been reported by Intartaglia *et al* [10]. In [11], the effect of different organic solvents on the size and PL quantum yield (QY) of the prepared Si nanoparticles has been investigated. In [12], the effect of different laser wavelength (532 and 1064 nm) on the absorption and solution concentration of colloidal Si solution has been studied in detail. The relationship between the pulse duration and size radius/size distribution has been investigated by Kuzmin *et al* [13].

Very recently, we successfully fabricated stable blue-emitting colloidal Si NCs in 1-hexene through a femtosecond (fs) LAL technique and demonstrated that the surfaces of the colloidal Si NCs have been well passivated by carbon chains as confirmed by Fourier transform infrared (FTIR) and x-ray photoelectron spectroscopy (XPS) spectra. The blue luminescence from colloidal Si NCs is attributed to the radiative recombination of the excitons formed at X or Γ ($\Gamma_{25} \rightarrow \Gamma'_{2}$) point via the surface states associated with the Si-C or Si-C-H₂ bonds [14]. Then, we carried out investigation on the effect of laser fluence on the structure and optical properties of colloidal Si NCs fabricated in 1-octadecene using fs laser ablation under different laser fluences. On the basis of the structural analysis, the Si NCs' surfaces have been passivated with carbon chains and oxygen; the passivation degree decreases gradually with the increase of laser fluence. The mechanism of violet and blue emission that peaked at around 3.25 and 2.86 eV from colloidal Si NCs has been assigned to the band-to-band direct recombination of electron-hole pairs in the quantum-confined colloidal Si NCs and radiative recombination of the localized excitons through oxygen-related surface states on the surface of the colloidal Si NCs, respectively [15].

The variable radiative recombination characteristics of electron-holes in quantum-confined colloidal Si NCs with surface chemistry can not only supply the means to identify the luminescence mechanism, but realize the possibility to control the origin of the luminescence. In this study, we present a detailed investigation of the effect of laser ablation time (LAT) on the micro-structure and luminescence of Si NCs, and we draw the following conclusions. (i) The variations in size of the prepared colloidal Si NCs between ~4.23–1.42 nm have been obtained by varying the LAT from 30 to 120 min. (ii) The blue PL bands at 405 and 430 nm are related to the electron-hole pair recombination associated with Si-C-H₂ and Si-O-Si vibration phonons, respectively. (iii) The measured PL QY is found to increase from 23.6% to 55.8% with extending the LAT from 30 to 120 min. The LAL technique provides a simple, flexible and less expensive way for the preparation of contamination-free NCs. This work is the sustainable investigation of the previous ones, and we wish to obtain the clear luminescence mechanism from colloidal Si NCs in combination with the results from different laser parameters (laser fluence, ablation time, laser

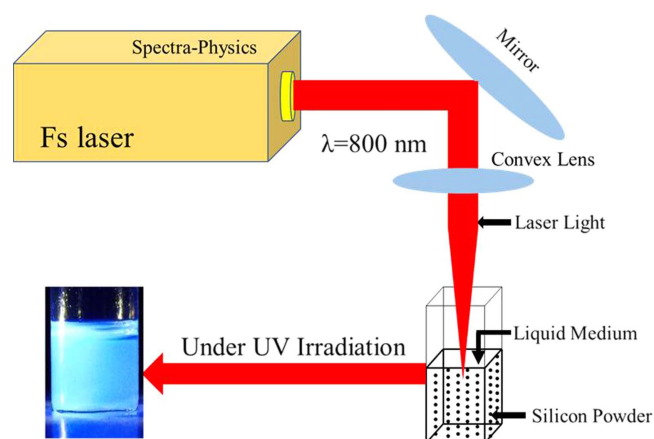


Figure 1. Schematic diagram of the experimental setup and PL photograph of the colloidal Si NC solution produced at LAT = 120 min.

wavelength, etc) to meet the application needs of the Si-based opto-electrical devices.

The preparation procedure of colloidal Si NC solution was described in detail in our previous works [14, 15]. In brief, the laser ablation experiments were carried out by using a Ti:sapphire fs laser system operated at 800 nm, with a pulse duration, laser fluence and frequency of 100 fs, 1.0 mJ cm⁻² and 80 MHz, respectively. The target materials are the mixture of porous Si powder with particle size ~120 nm (50 mg, Aladdin) and 1-octene (5.0 ml, >99%, Aladdin). The laser light beam, with a spot size 2.0 mm in diameter, was irradiated into the target solution through the lens with a focal length of 10 cm. During laser irradiation, the target mixture of porous Si powder and 1-octene solution was continuously stirred by a magnetic stirrer.

The prepared colloids were given the name S_x ($x = 1, 2, 3$ and 4) with LAT = 30, 60, 90 and 120 min, respectively. After finishing the ablation, the obtained yellowish solution was centrifuged at 12 000 rpm for 20 min, and the upper transparent colloidal Si NC solution was collected for structure and optical property measurements. The schematic diagram of the experimental setup and the photograph of the resultant blue-emitting colloidal Si NCs produced at LAT = 120 min are illustrated in figure 1.

The obtained colloidal solution was characterized by high-resolution transmission electron microscopy (HRTEM, JEOL JEM-2100F) and Raman microprobe spectra measurements (Jobin Yvon LabRAM HR 800 UV, 514.5 nm line of Ar⁺ laser). The UV-vis absorbance experiments were performed by using a Perkin-Elmer Lambda 20 spectrometer. The surface chemistry of the colloids was monitored by using a Fourier transform infrared (FTIR) spectrometer (Thermo Scientific, Nicolet iS 50) within a 400–4000 cm⁻¹ range. Using a Shimadzu Kratos Axis Ultra DLD spectrometer with a monochromatic Al K α x-ray source (1486.6 eV), we carried out the XPS measurements to characterize the surface bonding configurations for the sample Si NCs. Steady-state PL and PL excitation (PLE) spectra were recorded by a Hitachi High-Technologies F-7000 fluorescence spectrophotometer with an

excitation wavelength (λ_{exc}) of 370 nm. PL decay curves were measured through the excitation source with a 405.0 nm diode laser with a pulse width of 60.0 ps. The decay data at the nanosecond scale were recorded by using a time-correlated single-photon counting module.

We began with the HRTEM measurements for the formation and evolution of the Si NCs, as well as the density with LAT. The preparation and measurement procedures of the colloidal Si NCs were described in our previous work [15]. In brief, all the prepared Si NCs were purified rigorously using the mixture of solvent/antisolvent pairs (toluene/acetone) under ultrasound for 30 min to remove the redundant 1-octene. The obtained Si NCs were washed several times and then dried in a vacuum drying oven at 150 °C for 24 h. For preparing HRTEM measurements, the resultant clean Si NCs were decentralized in ethanol because of their high volatility. During the measurements, graphene was used as a support layer to obtain high-definition TEM images for the Si NCs.

Figures 2(a)–(d) show the TEM images for S1–S4. It can be clearly seen that the Si NCs are black dots that are well dispersed in 1-octene. The average dot size decreases gradually from around 4.23 nm in S1 with LAT = 30 min to ~1.42 nm in S4 under LAT = 120 min. Meanwhile, it can be calculated that the Si NC density enhances from $\sim 8.9 \times 10^{12}$ in S1 to $3.5 \times 10^{13} \text{ cm}^{-2}$ in S4. From TEM images of the Si NCs, the corresponding size statistics distribution was constructed by measuring the diameter of the Si NCs in around 200 nanoparticles, as shown in figures 2(a1)–(d1), which can be well fitted by Gaussian function. It can be observed that the Si nanoparticle size becomes small and the corresponding size distribution becomes narrow with increasing LAT. The mean diameters together with standard deviation for all the samples are summarized in table 1. The inset of figure 2(a) is a representative HRTEM image of a Si nanocrystal with lattice fringes of ~0.3 nm, corresponding to bulk Si (111) planes [16].

Raman analysis can further confirm the formation of ultra-small and crystalline Si NCs characterized by the broad Raman bands, as shown in figure 3(a). The Raman peaks fall in the range of 507 ~ 518 cm^{-1} for all the samples, where the position of the Si NCs always lies. The Raman peak position locates at ~518, 515, 511 and 507 cm^{-1} , and the corresponding full width at half maximum (FWHM) is ~11, 14, 28 and 37 cm^{-1} for the prepared samples S1–S4, respectively. The Raman peaks redshift and FWHM broadening occurs for all the samples with respect to those of Si wafer at 520 cm^{-1} (~3.4 cm^{-1}), which is attributed to the quantum confinement of the electronic wave function in the Si NCs, indicating that the characteristic dimension of the nanocrystal structure is less than 10 nm [11, 17, 18]. With increasing LAT, Raman peak energy shifts towards low energy and the linewidth of the Raman spectra becomes wide, suggesting the decrement of Si NC size. The relationship of the Raman peak position redshift ($\Delta\nu$, in cm^{-1}) with the Si NC size (d , in nm) can be expressed by the following equation [19]:

$$\Delta\nu = -19.856/d^{1.586}. \quad (1)$$

From equation (1), the calculated Si NC mean size is ~4.25, 3.14, 2.09 and 1.39 nm for S1–S4, respectively.

To investigate the effect of LAT on the size and production yield of Si NCs, UV–vis absorption spectra of colloidal Si NC solution produced at different LAT are depicted in figure 3(b). It can be obviously seen that the absorbance increases with increasing LAT. According to Beer–Lambert law [13]:

$$A = \varepsilon cl, \quad (2)$$

where A , ε , c and l are the absorbance, molar extinction coefficient, concentration of the solution and path length, respectively. During laser ablation, ε and l are fixed as constant. Thus, the absorbance is proportional to the concentration of the solution, and higher concentration can be expected under longer LAT. The obtained concentration of the colloid solution is ~2.0, 3.2, 4.1 and 4.8 mg ml^{-1} after laser ablation for 30, 60, 90 and 120 min, respectively. The increment of concentration can well explain the enhancement of Si NC density with increasing LAT (in figures 2(a)–(d)). Meanwhile, it can be observed that the absorption edge shifts to higher energy from ~320 in S1 to 250 nm in S4 with the increase of LAT, corresponding to energy values of ~3.87 and 4.96 eV, respectively. The bandgap energy of the Si NCs enhances with the decrease of their size owing to the quantum confinement effect (QCE). Therefore, the Si NCs with smaller size can be obtained under longer LAT.

In combination with TEM, Raman and UV–vis absorption measurements, the mean size of the nanoparticles decreases with the increase of LAT. The dependence of particle size on LAT can be explained as follows. (i) With prolonging LAT, the fragmentation would happen within the large-sized Si NCs during laser ablation. The fragmentation can involve the ejection of photoelectrons from the surface of the Si target, leaving positive charges on its surface. This induces the electrostatic repulsion between crystal faces with different crystal orientations, resulting in the fragmentation of a single larger-sized particle into several smaller ones [20].

(ii) According to the nucleation and growth theory [21]:

$$\Delta G\nu = -\frac{kT}{\Omega} \ln\left(\frac{C}{C_0}\right), \quad (3)$$

where $\Delta G\nu$, k , T , Ω and C_0 are the change of Gibbs free energy per unit volume of solid phase, Boltzmann constant, temperature, solute concentration and solubility, respectively. And also:

$$d_{\min} = -2\gamma/\Delta G\nu, \quad (4)$$

where, d_{\min} and γ represent the minimum size of the stable spherical nucleus and surface energy per unit area, respectively. Equation (4) is substituted into equation (3), which leads to:

$$d_{\min} = \frac{2\gamma}{kT} \ln\left(\frac{C_0}{C}\right). \quad (5)$$

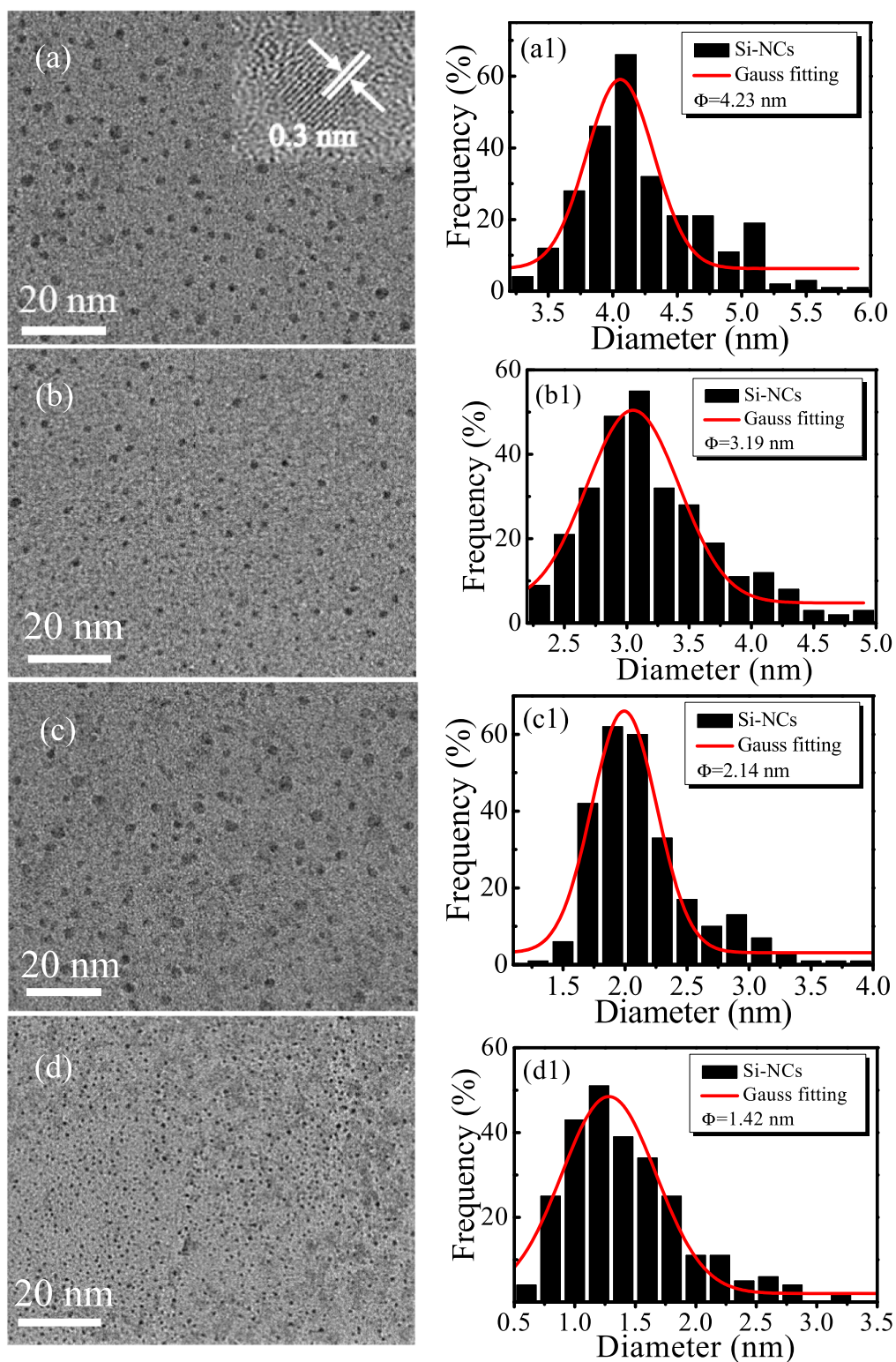


Figure 2. (a)–(d) and (a1)–(d1) TEM images and the corresponding size distribution of colloidal Si NCs. Inset: a typical HRTEM image of a Si NC. Φ , the mean size of the colloidal Si NCs.

Table 1. Average size and bandgap energy of Si NCs prepared under different LAT.

Sample no.	LAT (min)	Bandgap E_g (eV)	Average size (nm)	Standard deviation (nm)
1	30	1.60	4.23	4.05
2	60	1.66	3.19	3.17
3	90	1.73	2.14	2.01
4	120	1.83	1.42	1.39

From equation (5), we can conclude that the smaller-sized Si NC nuclei can be obtained from the colloid solution with higher concentration. Moreover, more nuclei can be formed with the enhancement of the solution concentration. This means that more Si nuclei will share the additionally provided Si atoms, resulting in smaller particle size under longer LAT.

Figure 4(a) (left) displays the FTIR spectra for all the samples, which can firsthand reveal the surface chemical bonding configuration of the Si NCs. The absorption bands at 1364, 2850, 2925 and 2960 cm^{-1} are attributed to the symmetric C–H₃ stretching, symmetric C–H₂ stretching, asymmetric C–H₂ stretching and asymmetric C–H₃ stretching mode, respectively [14, 22]. The absorption peaks at 670, 880, 1100 and 1460 cm^{-1} correspond to Si–C asymmetric vibration, Si–C symmetric vibration, Si–O–Si vibration and Si–CH₂ bending vibration, respectively [8, 23]. The clear Si–C asymmetric stretching vibration centered at $\sim 670 \text{ cm}^{-1}$ can be seen in figure 4(a) (right). The presence of Si–C bonds suggests that the surfaces of the Si NCs have been successfully passivated by carbon chains [14, 23]. The appearance of Si–O–Si bonds suggests that the surfaces of the Si NCs have been partly oxidized by oxygen dissolved in solution [24]. The scheme for the photo-assisted reaction between Si nanoparticles and 1-octene is shown in figure 4(b). The passivation mechanism of the Si NC surface with carbon and oxygen has been clarified in our previous work [15].

Figure 4(c) displays the densities of the Si–C and Si–O–Si bonds under different LAT, which can be calculated by integrating the absorption bands at 670 and 1100 cm^{-1} , respectively. It can be seen that the densities of the Si–O–Si bonds stay almost unchanged and the Si–C bond density increases with the increase of LAT. In general, the fs laser pulses unleash energy to electrons much faster than electron–phonon thermalization processes in the porous Si target, which can reduce local heating of the targets and keep the temperature of the colloidal solution stable during the laser ablation processes [11]. Therefore, the content of oxygen in the colloidal solution almost keeps a fixed value and the densities of the Si–O–Si bonds stay unchanged within the laser ablation. With extending LAT, on the one hand, more and more unstable C=C bonds will be broken, resulting in more surface passivation of Si with carbon free radical. On the other hand, the already large-sized Si NCs would be divided into several small-sized Si NCs due to the fragment, as confirmed by HRTEM measurements. Thus, smaller Si

NCs have more surface functional groups, leading to the increment of the Si–C bond densities with extending LAT [25].

We performed the XPS measurements to further characterize the surface structure for all the sample Si NCs, as shown in figure 5. The normalized experimental XPS spectra (hollow circles) can be well fitted by three Gaussian peaks (solid curves) locating at ~ 99.5 , 102.1 and 103.5 eV, respectively, corresponding to the characteristic of elemental Si, Si–C and Si–O bonding, respectively [26]. By integrating the fitting curves, we have calculated the densities of the Si–C and Si–O bonds for the sample Si NCs with different LAT. The density of the Si–C bonds increases and the Si–O bonds remain almost unchanged with LAT. These results indicate that the surfaces of colloidal Si NCs have been passivated by carbon chains and partly oxidized, well consistent with the FTIR results in figure 4(a).

Figure 6(a) shows the room-temperature PL spectra for all the samples with $\lambda_{\text{exc}} = 370 \text{ nm}$. It can be clearly observed that there are two obvious blue PL peaks at 405 (3.06 eV) and 430 nm (2.88 eV) together with FWHM 65 nm (0.33 eV) and 83 nm (0.42 eV) for all samples, respectively. Moreover, both emission peak energies remain unchanged with increasing LAT from 30 min in S1 to 120 min in S4. Meanwhile, there is a significant enhancement of the luminescence intensity by a factor of 8 with increasing LAT from 30 to 120 min. To understand the blue emission origin of the prepared samples, we first performed the temperature-dependent PL measurements within 83–300 K. Figure 6(b) shows the typical results for S4 with LAT = 120 min, where both the PL peak energies and corresponding FWHM remain unchanged within the measured range. Similar PL behavior has been reported in our previous work [14, 27]. These observations suggest that the origin of the light emission in the colloidal Si NCs is not from the QCE.

The colloidal Si NCs fabricated by laser ablation are confirmed to be indirect bandgap semiconductors due to the long absorbance band tail (see figure 3(b)). Figure 7(a) plots the absorption coefficient (a) as a function of the photon energy ($h\nu$). For indirect bandgap semiconductor, the dependence of energy on the absorption is given by the following equation:

$$a(h\nu)h\nu = A(h\nu - E_g)^2, \quad (6)$$

where A is a constant and E_g is the bandgap energy of the samples. The values of the bandgap energy for the colloidal Si NCs can be obtained by extrapolating the straight line portion of the $a(h\nu)$ versus $h\nu$ graph to the $h\nu$ axis (as illustrated in figure 7(a)), which exhibit 1.60, 1.66, 1.73 and 1.83 eV for the colloidal Si NC solution fabricated under 30, 60, 90 and 120 min of laser ablation, respectively (table 1). The values of the bandgap energy are smaller than those of the PL peak energies for all the samples. Thus, the band-to-band recombination in the Si nanoparticles can be safely excluded.

In order to clarify the light emission mechanism, we have further carried out PLE, λ_{exc} -dependent PL and time-resolved PL measurements for all the prepared samples. Figure 7(b) presents the representative λ_{exc} -dependent PL and PLE

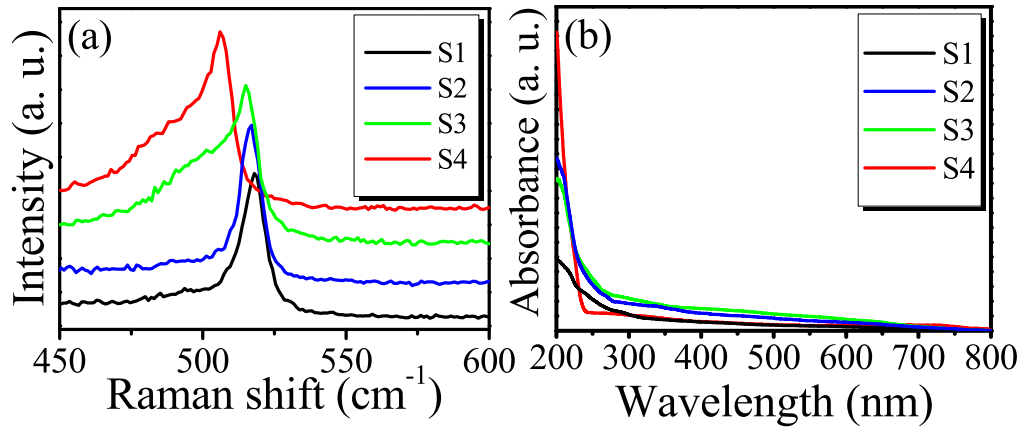


Figure 3. (a) Raman spectra of alkene-passivated Si NCs synthesized in 1-octene under different LAT: 30 (S1), 60 (S2), 90 (S3) and 120 min (S4). (b) UV-vis absorption spectra of S1-S4.

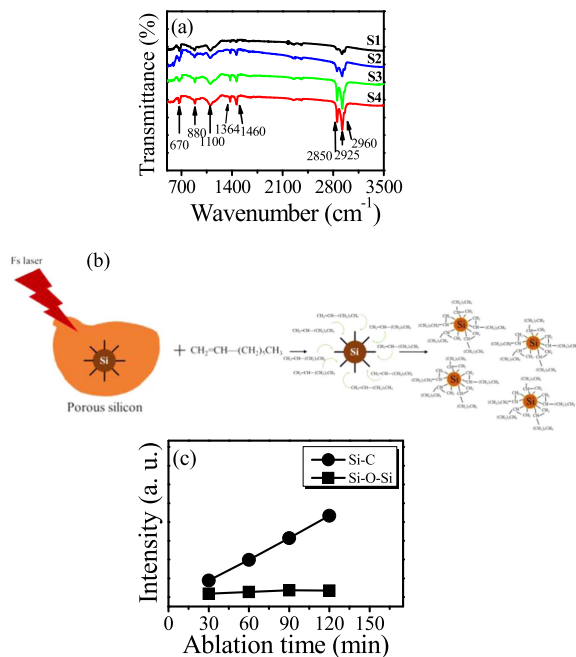


Figure 4. (a) Infrared transmittance spectra for all the colloidal Si NC samples (left) and FTIR spectra of Si-C bonds centered at 670 cm^{-1} (right), (b) schematic diagram for the formation processes of alkyl-terminated Si NC in organic solvent, and (c) density of Si-C and Si-O bonds as a function of LAT.

spectra of S4. We can see that the PL peak energies at 405 (3.06 eV) and 430 nm (2.88 eV) are independent of λ_{exc} throughout the measurement range. With increasing λ_{exc} , the emission intensity enhances significantly, and the luminescence intensity reaches the maximum for the colloidal Si NCs when excited at $\lambda_{\text{exc}} = 370\text{ nm}$ (3.35 eV). With the further increase of λ_{exc} over 370 nm, the luminescence intensity reduces drastically. The PLE spectra of S4 in figure 7(b) are monitored at emission peaks 405 (3.06 eV) and 430 nm (2.88 eV), respectively. The PLE peak position located at 370 nm (3.35 eV) is independent of detection wavelengths, indicating that the colloidal Si NCs absorb strongly at 370 nm and radiative de-excitation takes place at 405 and 430 nm [28].

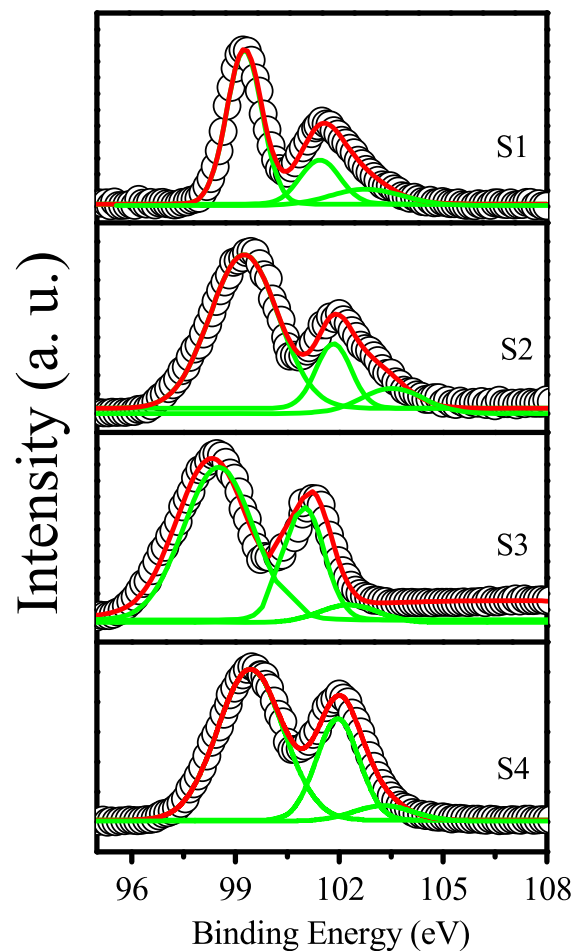


Figure 5. XPS spectra for all the sample Si NCs with different LAT.

Figure 7(c) shows the experimental (filled triangles and hollow squares) and fitted (solid curves) time-resolved PL spectra of S4 monitored at emission peaks of 405 and 430 nm, respectively. Both decay curves can be well fitted via a double-exponential iterative fitting program equipped by Edinburgh Instruments, by using double-exponential function:

$$I(t) = A_1 e^{-t/\tau_1} + A_2 e^{-t/\tau_2}, \quad (7)$$

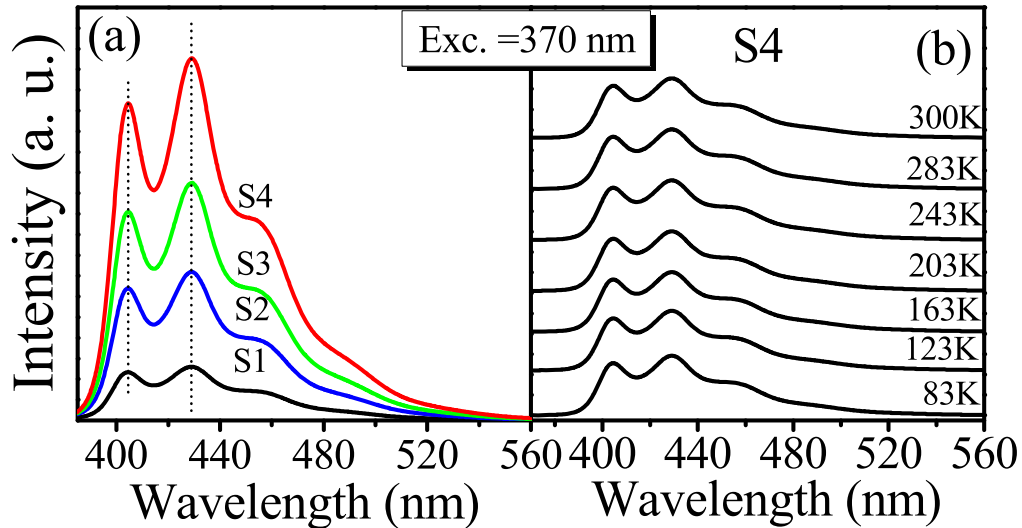


Figure 6. (a) Room-temperature PL spectra with $\lambda_{\text{exc}} = 370$ nm for all the samples and (b) temperature-dependent PL spectra of S4 with excitation wavelength 370 nm.

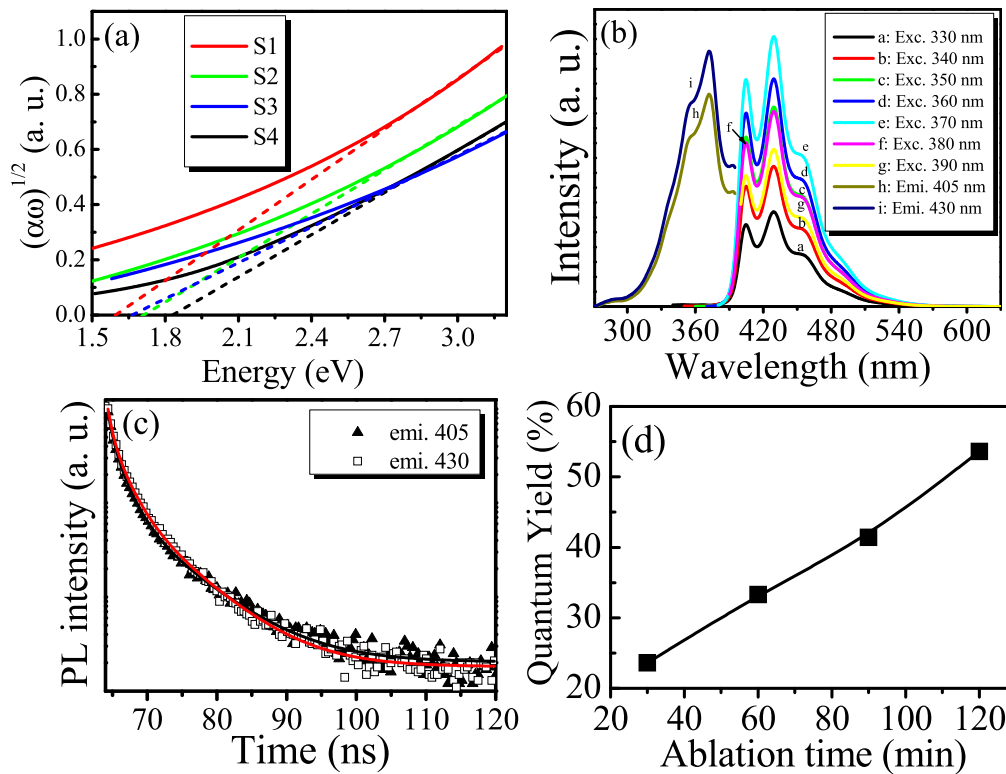


Figure 7. (a) Tauc plots of UV-vis spectra shown in figure 3(b) for all the fabricated samples. (b) Room-temperature PL at the indicated λ_{exc} and PLE spectra of all the samples. (c) Time-resolved PL spectra detected at 405 and 430 nm for S4. (d) PL QY measurements of all the samples.

where, $I(t)$ is the PL intensity as a function of time t ; A_1 , A_2 , τ_1 and τ_2 are the fitting constants. For emission peaks at 405 and 430 nm, $\tau_1 = 10.33$ ns ($A_1 = 1.04\%$), $\tau_2 = 1.63$ ns ($A_2 = 98.96\%$); $\tau_1' = 11.22$ ns ($A_1' = 1.32\%$), $\tau_2' = 1.73$ ns ($A_2' = 98.68\%$), respectively. With increasing LAT from 30 to 120 min, the colloidal solution exhibits a fast

decay lifetime from 4.35 to 1.63 ns and a slow one from 15.56 to 10.33 ns for the emission peak at 405 nm, respectively. Meanwhile, a short decay lifetime from 4.68 to 1.73 ns and a long one from 14.37 to 11.22 ns with detection PL peak energy at 430 nm are obtained for S1–S4, respectively. The average decay lifetime $\bar{\tau}$ can be calculated

in the light of the following equation:

$$\bar{\tau} = (A_1\tau_1^2 + A_2\tau_2^2)/(A_1\tau_1 + A_2\tau_2). \quad (8)$$

With increasing LAT, $\bar{\tau}$ decreases from 5.22 to 3.63 ns and from 5.35 to 3.72 ns in S1–S4 for detection PL peak energy at 405 and 430 nm, respectively. Owing to much stronger QCE in the colloidal Si NCs with smaller size than that in large ones, the order of nanosecond decay lifetime decreases significantly with decreasing Si NC size, resulting in the enhancement of the radiative recombination rate.

As reported in figure 6(a), when excited with 370 nm, two PL bands at 405 and 430 nm can be observed for all samples. Both emissions consist of a band peaked around 370 nm as the excitation profiles shown in figure 7(b). Similar excitation behavior has been reported in [29]. These findings suggest that the excitation transition occurs between levels localized at the same defect. Based on the comparison with our previous literature data, both PL bands are related to oxygen-deficient centers in the oxidized Si NCs [15]. The fast 405 nm (3.06 eV) and 430 nm (2.88 eV) PL bands are the inverse of the 370 nm (3.35 eV) excitation, and the Stoke shifts of 0.29 and 0.42 eV for the 405 and 430 nm PL bands are assigned to the electron–phonon coupling. On the basis of the configuration coordinate mode, the coupling energy of phonons can be expressed as follows [14]:

$$\hbar\Omega = W^2|_{T \rightarrow 0}/(4 \ln 2)E_s, \quad (9)$$

where W is the FWHM of the PL spectrum and it remains unchanged throughout the measurement temperature range as in figure 6(b). E_s is the Stokes shift of the PL band. The calculated phonon energy $\hbar\Omega$ is ~ 0.11 and 0.14 eV for the PL bands peaked at 405 and 430 nm, equivalent to ~ 880 and 1100 cm^{-1} , respectively. The values of phonon energy relate well to the Si–C–H₂ and Si–O–Si vibration modes shown in figure 4(a), respectively. This implies that the origin of blue PL bands relates to the electron–hole pair recombination associated with Si–C–H₂ and Si–O–Si vibration phonons for 405 and 430 nm, respectively. Based on the above discussions, we propose that the room-temperature blue emissions that peaked at 405 and 430 nm originate from the radiative recombination of electron–hole pairs via the oxygen-deficient centers related to the Si–C–H₂ and Si–O–Si bonds of the colloidal Si NCs prepared in 1-octene, respectively.

To further investigate the optical characteristic of the colloidal Si NCs synthesized by fs laser in solution, the PL QY measurements of the produced colloidal Si NC solution were performed at room-temperature using the PL QY measurement system QuantaMaster 40 with a 150 W Xe lamp coupled to a monochromator for wavelength discrimination. PL QY can quantitatively account for absorption and emission, reflection and scattering effects. In order to prepare the Si NC samples for the PL QY measurements, two colloids were dropped on Si wafers and dried inside a fume hood for 90 min. The dried Si NCs were then placed inside an integrating sphere, and a multichannel analyzer was used for signal detection. The PL QY value of the samples can be

calculated using the following equation:

$$QY = N_E/N_A = (L_{\text{sample}} - L_{\text{blank}})/(E_{\text{blank}} - E_{\text{sample}}), \quad (10)$$

where N_E , N_A means the emitted photons and absorbed photons, respectively; E_{sample} , E_{blank} represent the sample and blank integrated spectra of the excitation beam, respectively; L_{sample} is the integrated spectra of the sample's luminescent wavelength range. For the case of solution measurements, a cuvette filled with the solvent was used as the blank, and L_{blank} denotes the integrated spectra of a cuvette filled with solvent inside the integrating sphere [30].

Figure 7(d) gives the PL QY values of all the samples, where the PL QY shows an improvement from 23.6% to 55.8% with increasing LAT from 30 to 120 min. With increasing LAT, first, the surface passivation of the colloidal Si NCs shows a significant improvement (see figure 4(c)), leading to fewer non-radiative centers and smaller non-radiative rate. The dependence of PL QY on the radiative/non-radiative rate can be described by the following equation [12]:

$$QY = K_r/(K_r + K_{nr}), \quad (11)$$

where, K_r and K_{nr} represent the radiative and non-radiative rate, respectively. K_r remains almost unchanged, while K_{nr} is remarkably decreased owing to the good surface passivation. Second, the average size of the colloidal Si NCs decreases significantly with the increase of LAT, as confirmed in figures 2 and 3(a), and more and more carriers in much smaller quantum-confined Si NCs can be easily excited. Third, the number of colloidal Si NCs enhances from S1 to S4 with increasing LAT from 30 to 120 min (see figures 2(a)–(d)), leading to the production of a large number of luminescent centers. Therefore, higher PL QY is expected to be obtained with extending the LAT.

In conclusion, we have performed an overall investigation on the structure and optical properties of the colloidal Si NCs produced under different LAT. Raman, HRTEM, FTIR and XPS measurements demonstrate that the mean diameter of the colloidal Si NCs decreases from ~ 4.23 to 1.42 nm with extending LAT from 30 to 120 min, and the surface passivation of the Si NCs with carbon chains is enhanced and the oxidization remains almost unchanged when increasing LAT. In combination with the room-temperature PL, PLE and time-resolved PL spectra, we deduce that the room-temperature blue emissions that peaked at 405 and 430 nm originate from the radiative recombination of electron–hole pairs via the oxygen-deficient centers related to the Si–C–H₂ and Si–O–Si bonds of the colloidal Si NCs prepared in 1-octene, respectively. Due to the good surface passivation and increased density of the colloidal Si NCs, the PL QY increases significantly with extending the ablation time.

Acknowledgments

The authors thank the National Natural Science Foundation of China for the financial support (Grant Nos. 11504229 and 61234005).

ORCID iDs

H L Hao  <https://orcid.org/0000-0001-5446-5071>

References

- [1] Angi A, Sinelnikov R, Meldrum A, Veinot J G C, Balverg I, Azulay D, Millo O and Rieger B 2016 Photoluminescence through in-gap states in phenylacetylene functionalized silicon nanocrystals *Nanoscale* **8** 7849–53
- [2] Gu W *et al* 2017 Silicon-quantum-dot light-emitting diodes with interlayer-enhanced hole transport *IEEE Photonics J.* **9** 4500610
- [3] Yu T, Wang F, Xu Y, Ma L L, Pi X D and Yang D R 2016 Graphene coupled with silicon quantum dots for high-performance bulk-silicon-based Schottky-junction photodetectors *Adv. Mater.* **28** 4912–9
- [4] Maier-Flaig F, Rinck J, Stephan M, Bockrocker T, Bruns M, Kübel C, Powell A K, Ozin G A and Lemmer U 2013 Multicolor silicon light-emitting diodes (Si LEDs) *Nano Lett.* **13** 475–80
- [5] Wu S C, Zhong Y L, Zhou Y F, Song B, Chu B B, Ji X Y, Wu Y Y, Su Y Y and He Y 2015 Biomimetic preparation and dual-color bioimaging of fluorescent silicon nanoparticles *J. Am. Chem. Soc.* **137** 14726–32
- [6] Zhong Y L, Sun X T, Wang S Y, Peng F, Bao F, Su Y U, Li Y Y, Lee S T and He Y 2015 Facile, large-quantity synthesis of stable, tunable-color silicon nanoparticles and their application for long-term cellular imaging *ACS Nano* **9** 5958–67
- [7] Dasog M, De los Reyes G B, Titova L V, Hegmann F A and Veinot J G C 2014 Size vs surface: tuning the photoluminescence of freestanding silicon nanocrystals across the visible spectrum via surface groups *ACS Nano* **8** 9636–48
- [8] Nakamura T, Yuan Z, Watanabe K and Adachi S 2016 Bright and multicolor luminescent colloidal Si nanocrystals prepared by pulsed laser ablation in liquid *Appl. Phys. Lett.* **108** 023105
- [9] Dohnalová K, Gregorkiewicz T and Kůsová K 2014 Silicon quantum dots: surface matters *J. Phys. Condens. Mat.* **26** 173201
- [10] Intartaglia R, Bagga K, Brandi F, Das G, Genovese A, Di Fabrizio E and Diaspro A 2011 Optical properties of femtosecond laser-synthesized silicon nanoparticles in deionized water *J. Phys. Chem. C* **115** 5102–7
- [11] Xin Y Z, Kitasako T, Maeda M and Saitow K 2017 Solvent dependence of laser-synthesized blue-emitting Si nanoparticles: size, quantum yield, and aging performance *Chem. Phys. Lett.* **674** 90–7
- [12] Chewchinda P, Tsuge T, Funakubo H, Odawara O and Wada H 2013 Laser wavelength effect on size and morphology of silicon nanoparticles prepared by laser ablation in liquid *Jpn. J. Appl. Phys.* **52** 025001
- [13] Kuzmin P G, Shafeev G A, Bukin V V, Garnov S V, Farcau C, Carles R, Warot-Fontrose B, Guieu V and Viau G 2010 Silicon nanoparticles produced by femtosecond laser ablation in ethanol: size control, structural characterization, and optical properties *J. Phys. Chem. C* **114** 15266–73
- [14] Hao H L, Wu W S, Zhang Y, Wu L K and Shen W Z 2016 Origin of blue photoluminescence from colloidal silicon nanocrystals fabricated by femtosecond laser ablation in solution *Nanotechnology* **27** 325702
- [15] Wu W S, Hao H L, Zhang Y X, Li J, Wang J J and Shen W Z 2018 Correlation between luminescence and structural evolution of colloidal silicon nanocrystals synthesized under different laser fluences *Nanotechnology* **29** 025709
- [16] Nakamura T, Yuan Z and Adachi S 2014 Luminescent silicon nanocrystals produced by near-infrared nanosecond pulsed laser ablation in water *Nanotechnology* **25** 275602
- [17] Rodio M, Brescia R, Diaspro A and Intartaglia R 2016 Direct surface modification of ligand-free silicon quantum dots prepared by femtosecond laser ablation in deionized water *J. Colloid Interf. Sci.* **465** 242–8
- [18] Faraci G, Gibilisco S, Russo P and Pennisi A R 2006 Modified Raman confinement model for Si nanocrystals *Phys. Rev. B* **73** 033307
- [19] Vaccaro L, Sciortino L, Messina F, Buscarino G, Agnello S and Cannas M 2014 High-yield preparation of blue-emitting colloidal Si nanocrystals by selective laser ablation of porous silicon in liquid *Appl. Surf. Sci.* **302** 62–5
- [20] Singh S C, Mishra S K, Srivastava R K and Gopal R 2010 Optical properties of selenium quantum dots produced with laser ablation of water suspended Se nanoparticles *J. Phys. Chem. C* **114** 17374–84
- [21] Cao G Z 2004 *Nanostructures and Nanomaterials: Synthesis, Properties, and Applications* (London: Imperial College Press)
- [22] Zou J, Baldwin R K, Pettigrew K A and Kauzlarich S M 2004 Solution synthesis of ultrastable luminescent siloxane-coated silicon nanoparticles *Nano Lett.* **4** 1181–6
- [23] Mardanian M, Tarasenko N V and Nevar A A 2014 Influence of liquid medium on optical characteristics of the Si nanoparticles prepared by submerged electrical spark discharge *Braz. J. Phys.* **44** 240–6
- [24] Tan D Z, Ma Z J, Xu B B, Dai Y, Ma G H, He M, Jin Z M and Qiu J R 2011 Surface passivated silicon nanocrystals with stable luminescence synthesized by femtosecond laser ablation in solution *Phys. Chem. Chem. Phys.* **13** 20255–61
- [25] Nguyen V, Yan L H, Si J H and Hou X 2015 Femtosecond laser-induced size reduction of carbon nanodots in solution: effect of laser fluence, spot size, and ablation time *J. Appl. Phys.* **117** 084304
- [26] Hessel C M, Reid D, Panthani M G, Rasch M R, Goodfellow B W, Wei J, Fujii H, Akhavan V and Korgel B A 2012 Synthesis of ligand-stabilized silicon nanocrystals with size-dependent photoluminescence spanning visible to near-infrared wavelengths *Chem. Mater.* **24** 393
- [27] Hao H L and Shen W Z 2008 Identification and control of the the origin of photoluminescence from silicon quantum dots *Nanotechnology* **19** 455704
- [28] Chaturvedi A, Joshi M P, Rani E, Ingale A, Srivastava A K and Kukreja L M 2014 On red-shift of UV photoluminescence with decreasing size of silicon nanoparticles embedded in SiO₂ matrix grown by pulsed laser deposition *J. Lumin.* **154** 178–84
- [29] Vaccaro L, Sciortino L, Messina F, Buscarino G, Agnello S and Cannas M 2014 Luminescent silicon nanocrystals produced by near-infrared nanosecond pulsed laser ablation in water *Appl. Surf. Sci.* **302** 62–5
- [30] Makowiecki J and Martynski T 2014 Absolute photoluminescence quantum yield of perylene dye ultra-thin films *Org. Electron.* **15** 2395–9